Spectral properties of GX 339−4 in the intermediate state using *AstroSat* observation

Arghajit Jana [1,2]★ Debjit Chatterjee [3] Hsiang-Kuang Chang [1] Sachindra Naik [4]
and Santanu Mondal [3]

[1]*Institute of Astronomy, National Tsing Hua University, Hsinchu 300044, Taiwan*
[2]*Instituto de Estudios Astrofísicos, Facultad de Ingeniería y Ciencias, Universidad Diego Portales, Av. Ejército Libertador 441, Santiago, Chile*
[3]*Indian Institute of Astrophysics, II Block Koramangala, Bangalore 560034, India*
[4]*Astronomy & Astrophysics Division, Physical Research Laboratory, Navrangpura, Ahmedabad 380 009, India*

ABSTRACT

We present the results obtained from the spectral studies of black hole X-ray binary GX 339−4 using *AstroSat* observations during its 2021 outburst. *AstroSat* observed the source in the intermediate state for ∼600 ks. The combined spectra of SXT and LAXPC in the 0.7−25 keV energy range are studied with phenomenological and physical models. The spectral study reveals a receding disc and a contracting corona during the observation period. The outflow rate is found to be increased though the accretion rates did not vary during the observation period. The X-ray flux decreases as the disc recedes and the spectrum becomes hard. At the same time, the Comptonized flux decreases with increasing fraction of thermal emission. This could be plausible that episodic jet ejection modified the corona and reduced Comptonized flux. An iron emission line at 6.4 keV is observed in the spectra of all the orbits of observation. We find that the equivalent width of the iron emission line correlates with the photon index, indicating a decrease in the reflection strength as the spectrum becomes hard. We observe that the disc flux does not follow $F_{DBB} - T^4$ relation.

Key words: accretion, accretion discs – stars: black holes – stars: individual: (GX 339–4) – X-rays: binaries.

1 INTRODUCTION

An X-ray spectrum of an outbursting black hole X-ray binary (BHXB) can be approximated by a multicolour blackbody (MCD) component and a power-law (PL) tail. The MCD emission is believed to be originated in a geometrically thin and optically thick accretion disc (Shakura & Sunyaev 1973), while the hard PL tail originates in a Compton corona, located close to the BH (e.g. Haardt & Maraschi 1993; Chakrabarti & Titarchuk 1995; Done, Gierliński & Kubota 2007). A fraction of the seed photons get up-scattered with the hot electrons of the Compton corona and produce a PL tail via inverse-Comptonization (Sunyaev & Titarchuk 1980, 1985). Further, a fraction of the hard photons are reprocessed in the disc and produce an iron K line at ∼6.4 keV and a reflection hump at ∼20−40 keV (Fabian et al. 1989; Matt, Perola & Piro 1991).

An outbursting BHXB commonly shows two major spectral states such as low–hard state (LHS) and high–soft state (HSS). A BHXB transits from the LHS to HSS or vice-versa through an intermediate state (IMS). A cool disc of temperature $T_{in} \sim 0.1−0.5$ keV, and photon index, $\Gamma \sim 1.5−1.7$ characterizes the X-ray spectrum in the LHS. In the LHS, the hard X-ray flux dominates over the soft X-ray flux. An evolving type-C quasi periodic oscillation (QPO) is observed in the LHS along with a compact and stable jet (e.g. Nandi

et al. 2001; Fender & Belloni 2004) which can significantly modify the shape of the spectrum and the accretion geometry. In the HSS, the X-ray spectrum can be characterized by a disc of temperature, $T_{in} \sim$ 1 keV and the $\Gamma \geq 2.3$. The soft X-ray flux dominates over the hard X-ray flux in the HSS. No jet or low-frequency QPO (LFQPO) is observed in the HSS. In the state transition phase or the IMS, the hard X-ray and soft X-ray fluxes are comparable. The X-ray spectrum is characterized by a disc of temperature $T_{in} \sim 0.5−1$ keV and $\Gamma \sim 2$. A discrete or episodic jet is seen in the IMS. In the IMS, a sporadic type-B and type-A QPOs are observed. One may further divide the IMS as hard−intermediate state (HIMS) and soft–intermediate state (SIMS). The HIMS spectra are generally charatarized by photon index of ∼1.8−2, with the hard X-ray flux dominates. In the SIMS, the soft X-ray flux dominates over the hard X-ray flux, with the photon index ∼2−2.2 and $T_{in} \sim 0.8−1$ keV.

GX 339−4 was first observed in 1973 (Markert et al. 1973) with the 1−60 keV MIT X-ray detector onboard OSO-7 satellite. Parker et al. (2016) suggested the mass of the BH as $9.0^{+1.6}_{-1.2}M_\odot$, while Sreehari et al. (2019) estimated the mass in the range of 8.3−11.9 M$_\odot$. The distance of the source is estimated to be $d = 8.4 \pm 0.9$ kpc (Parker et al. 2016). As GX 339−4 is a non-eclipsing binary, the inclination angle should be <60º (Cowley et al. 2002). Zdziarski, Ziółkowski & Mikołajewska (2019) estimated a lower limit of the inclination as 40º from the secondary mass function. Joint modelling of *Suzaku*, *XMM-Newton*, and *NuSTAR* observations was used by Miller et al. (2008); Mondal, Chakrabarti & Debnath (2016) to

★ E-mail: argha0004@gmail.com

explain the relativistic broadening of the Fe K α line and inferred that the source is a highly spinning (≥ 0.93) black hole. A distorted Fe K α line above the continuum is observed in the *RXTE* and *XMM-Newton* data suggesting a high spin parameter for the black hole (Reis et al. 2008; Plant et al. 2014). Thus, it is evident that the source is extremely spinning, though the exact values of the disc inclination and distance to the source are a topic of intense research.

There are extensive discussions on the origin of temporal, spectral, and multiwavelength properties of the source during different outbursts using observations with different satellites (Dinçer et al. 2012; Nandi et al. 2012; Bachetti et al. 2015; Basak & Zdziarski 2016). Most of the works reached at the conclusion that the spectra of GX 339−4 can be well explained by considering a cold thermal disc, hot corona, and a reflection component. In addition, a Gaussian component is needed to fit the Fe K α line, which is believed to be originated from reflection. However, this source showed a positive correlation between the equivalent width (EW) and mass accretion or photon index (Γ; see Tomsick et al. 2009; Debnath, Mondal & Chakrabarti 2015), which is somewhat opposite from what numerical simulation predicts (Zycki & Czerny 1994; García et al. 2013; Mondal, Adhikari & Singh 2021). Such positive correlation can be observed if the disc moves inward (increasing Γ), thereby increasing the number of hard photons intercepted in the disc, which increases the reflection; hence, the EW increases (e.g. Zdziarski, Lubiński & Smith 1999).

GX 339−4 showed a long X-ray outburst in 2021, which lasted for about 10 mon (Corbel et al. 2021; Pal et al. 2021). The outburst was extensively studied with several X-ray observatories, such as *Swift* (Pal et al. 2021), *NuSTAR* (Garcia et al. 2021), *NICER* (Wang et al. 2021), *Insight-HXMT* (Liu et al. 2021), *INTEGRAL* (Ferrigno et al. 2021), and *AstroSat* (Husain et al. 2021). The source was also studied in the optical (Saikia et al. 2021) and radio wavebands (Husain et al. 2021). Using *Insight-HXMT*, Liu et al. (2022) studied the source during its hard-to-soft state transition. Stiele & Kong (2023) studied the evolution of the type-B QPO using the *NICER* observation. Yang et al. (2023) investigated the type-B QPO and fast variability of the source during the state transition using *Insight-HXMT* observation. Using the time-averaged spectra of *AstroSat* and *NICER*, Peirano et al. (2023) suggested of a dual corona in the source.

In general, the accretion dynamics is well-studied in the LHS and HSS. However, it is not well-understood in the IMS (e.g. Jana 2022). It is believed that the accretion geometry changes significantly during the IMS (e.g. Gardner & Done 2013; Yang et al. 2015; Jana et al. 2022). The presence of the discrete ejection also makes the IMS complex. To understand the IMS better, we studied the well-known BHXB GX 339−4 in the IMS during its 2021 outburst in this paper. *AstroSat* observed GX 3394 in the IMS between 2021 March 30 and April 6 for an exposure of 600 ks. Although, Peirano et al. (2023) studied the same *AstroSat* observation, they studied the spectrum only obtained on 2021 March 30. Here, we used all the data obtained from the entire *AstroSat* observation from 2021 March 30 to April 6. The timing properties of the source are presented in Mondal et al. (2023). In this paper, we present the results obtained from the spectral analysis of the source in the IMS. The paper is organized in the following way. In Section 2, we present the observations and data extraction processes. The analysis and results are presented Section 3. In Section 4, we discuss our findings. Finally, in Section 5, we summarize our findings.

2 OBSERVATION AND DATA REDUCTION

AstroSat is the first Indian multiwavelength astronomical satellite that provides a broad-band coverage from optical to hard X-ray bands

for exploring the nature of the cosmic sources (Agrawal 2006). It consists of five sets of instruments, namely Soft X-ray Telescope (SXT; Singh et al. 2017), Large Area X-ray Proportional Counters (LAXPC; Antia et al. 2017), Cadmium Zinc Telluride Imager (CZTI; Rao et al. 2017), a Scanning Sky Monitor (Ramadevi et al. 2018), and Ultraviolet Imaging Telescope (UVIT; Tandon et al. 2017), onboard the satellite. In this work, we used data from the SXT and LAXPC.

The SXT is a soft X-ray focusing telescope that works in 0.3−8 keV energy range. The effective area and energy resolution of the instrument are 128 cm^2 and 5−6 per cent at 1.5 keV and 22 cm^2 and 2.5 per cent at 6 keV, respectively. GX 339−4 was observed with SXT in the photon counting (PC) mode, at a time resolution of 2.4 s. The level-1 data were reprocessed using standard SXT pipeline software AS1SXTLEVEL 12−1.4B1 to obtain cleaned event files from each orbit of observation. As the source was bright in soft X-rays (count rate of >40 count sec^{-1}), the SXT data are affected due to photon pile-up. To avoid the pile-up effect, we chose an annular region with a fixed outer radius of 10 arcmin and a variable inner radius. The pile-up was checked from the spectral distortion. We found that the pile-up effect was removed when the inner radius of 8 arcmin is considered in our analysis. We used background spectra and response matrix files that are supplied by the SXT instrument team. Using SXTARFMODULE tools, the auxiliary response files (ARF) are generated. In this work, we used SXT spectra in the 0.7−7.0 keV range.

AstroSat has three LAXPC units that are sensitive to the X-ray photons in 3−80 keV energy range, with a total effective area of 8000 cm^2 at 15 keV. The timing and spectral resolutions of the LAXPC are 10 μs and 12 per cent at 22 keV, respectively. In our analysis, we used only event mode data from LAXPC20 unit. Due to high background and gain issues with the instruments, we did not use data from LAXPC10 and LAXPC30 (Antia et al. 2017, 2021). We extracted spectra, background spectra, and response matrices using standard data analysis tools LAXPCSOFTWARE (LAXPCSOFT; version 2022 August 15). We used LAXPC spectra in the 3−25 keV energy range in our analysis. We did not use spectra above 25 keV as the data are background dominated above 25 keV.

3 ANALYSIS AND RESULTS

3.1 Outburst profile

GX 339–4 showed an outburst in the first week of 2021 January that lasted for about 10 mon. The 2021 outburst was extensively monitored in multiwavelength bands. We show the outburst profile of GX 339–4 during the 2021 outburst in Fig. 1. In the top three panels, we show the variation of MAXI/GSC light curves in (a) 2−20 keV, (b) 2−4 keV, and (c) 4−20 keV energy ranges, respectively. In the bottom panel of Fig. 1, we show the variation of hardness ratio (HR). The HR is defined as the ratio of the count rate in the 4−20 keV range to the count rate in the 2−4 keV range.

At the beginning of the outburst, the count rate increases rapidly in all energy bands till 2021 February 18 (MJD 59263). Later, the count rate increased slowly till 2021 March 20 (MJD 59293). Then, the soft X-ray (2−4 keV energy band) count rate increased rapidly till 2021 March 30 (MJD 59303), although the hard X-ray count rate did not change. As a result, the HR decreased sharply as the source entered the IMS. Then, the count rate in all energy bands decreased sharply, showing an alternative flux profile (AFP) similar to the 'flip-flop' profile (FFP) nature of the light curve between 2021 March 30 (MJD 59303) and 2021 April 10 (MJD 59314; see Mondal et al. 2023 for details). The AFP is also seen in a shorter time-scale on MJD 59305–59306. Since MJD 59308, the soft X-ray count rate increased rapidly
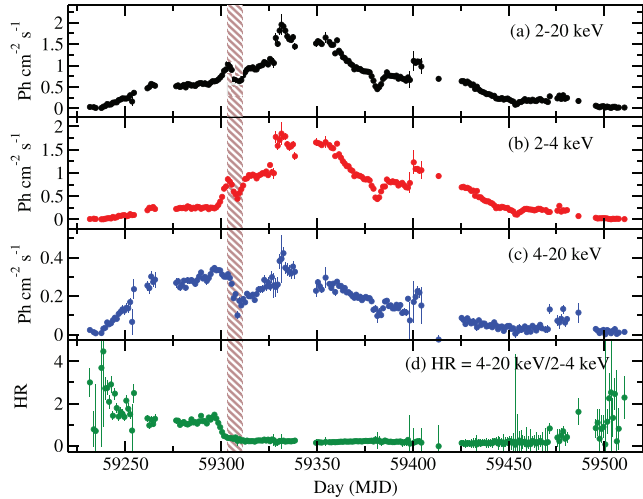
Figure 1. Outburst profile of GX 339–4 during the 2021 outburst. The variation of (a) 2−20 keV count rate, (b) 2−4 keV count rate, (c) 4−20 keV count rate, and (d) hardness ratio (count rate in 4−20 keV range/count rate in 2−4 keV range) are shown. The light curves are obtained from MAXI/GSC. The shaded grey region marks the duration of the *AstroSat* observation of the source.

compared to the hard X-ray band. On 2021 April 4 (MJD 59331), the X-ray flux attained its peak as the source entered the HSS.

After 2021 April 4, the source entered the declining phase of the outburst as both soft X-ray and hard X-ray count rates decreased slowly till 2021 July 3 (MJD 59398). Another AFP was observed in the declining phase between 2021 June 12 (MJD 59377) and 2021 June 21 (MJD 59386). A sudden increase in the X-ray count rate was observed after 2021 July 3. Following that, the X-ray intensity slowly decreased till 2021 September 13 (MJD 59470). The HR was observed to be constant till that day. Thereafter, the HR increased, indicating the source moved to the IMS. After 2021 September 29 (MJD 59486), the source was observed to be in the LHS as the HR increased and the X-ray count rate decreased further. GX 339–4 remained in the LHS till the end of the outburst.

3.2 Spectral analysis

We used combined 0.7−7 keV SXT and 3−25 keV LAXPC data for both orbit-wise and day-wise spectral study. We carried out the spectral analysis in 0.7−25 keV energy range in HEASEARC's spectral analysis software package XSPEC v12.10 (Arnaud 1996). We used both phenomenological and physical models to study the spectral properties of the source. The orbit-wise spectra are studied with phenomenological models, while the day-wise spectra are studied with the physical models. For the phenomenological model, we used the simple DISKBB (Mitsuda et al. 1984; Makishima et al. 1986) plus NTHCOMP model (Zdziarski, Johnson & Magdziarz 1996; Życki, Done & Smith 1999) to fit the spectrum. For the physical model, we used the relativistic reflection model RELXILLLP (García et al. 2013; Dauser et al. 2016), and JETCAF (Chakrabarti & Titarchuk 1995; Mondal & Chakrabarti 2021) model in our fitting.

3.2.1 Phenomenological model

We started our analysis with the phenomenological two-component model (hereafter Model-1): thermal MCB emission and Comptonized emission for the spectral fitting. The thermal and non-

thermal emissions were modelled by DISKBB and NTHCOMP in XSPEC, respectively. Along with these, we also used TBABS and a GAUSSIAN function for the Galactic absorption and iron Kα emission line, respectively. We fixed the Gaussian line energy at 6.4 keV. During the fitting, we tied the seed photon temperature (kT_{bb}) of NTHCOMP with the inner disc temperature (T_{in}) of the DISKBB model. Initially, we kept the hot electron temperature (kT_e) free. However, we could not constrain it. Thus, we kept the kT_e frozen at 50 keV during the spectral analysis. We used WILM abundances (Wilms, Allen & McCray 2000) and cross-section of Verner et al. (1996) in our analysis. We added a systematic of 3 per cent while fitting the data (e.g. Antia et al. 2021). We also applied a gain correction to the SXT spectra with a fixed slope of 1 to flatten the residuals at 1.8 and 2.2 keV using GAIN FIT command in XSPEC.

From the DISKBB normalization (N_{DBB}), we calculated the inner disc radius (R_{in}). The R_{in} is related to the N_{DBB} as $N_{DBB} = (r_{in}/D_{10}^2)\cos\theta$, where r_{in} is the apparent disc radius in km, D_{10} is the source distance in the unit of 10 kpc, and θ is the inclination angle. The inner radius of the disc (R_{in}) is given by, $R_{in} = \xi\kappa^2 r_{in}$, where $\xi = 0.41$ is the correction factor (Kubota et al. 1998), and $\kappa = 1.7-2.0$ is the spectral hardening factor (Shimura & Takahara 1995). Here, we calculated R_{in}, considering $\kappa = 1.8$, $\theta = 30$ degrees, and $d = 8.4 \pm 0.9$ kpc (Parker et al. 2016). For the iron emission line, we calculated the equivalent width (EW) in XSPEC using EQW command. Using CFLUX, we calculated absorption corrected flux for each of the three components. We calculated the disc flux (F_{DBB}), iron line flux (F_{Ga}), and Comptonized flux (F_{PL}) in the range of 0.001−10, 0.1−10 and 0.1−500 keV, respectively. We also considered a high-energy cutoff at 200 keV while calculating F_{PL}. The total flux (F_{tot}) is calculated as $F_{tot} = F_{DBB} + F_{PL} + F_{Ga}$. We also estimated the fraction of thermal emission as $f_{disc} = F_{DBB}/F_{tot}$. The detailed spectral analysis results are tabulated in Table A1.

We obtained good fits for all orbits-wise spectra with the Model-1. The left panel of Fig. 2 shows the best-fitting spectra for orbit 29 755 (MJD 59303.12), fitted with Model-1. The residual is shown in the bottom panel. The red and blue points represent the SXT and LAXPC data, respectively. The black dashed, grey solid, dark green solid, and magenta lines represent the total emission, Comptonized emission (NTHCOMP), disc-blackbody (DISKBB) and iron emission line (GAUSSIAN), respectively. We show the variation of (a) line-of-sight hydrogen column density (N_H) in 10^{22} cm^{-2}, (b) inner disc temperature (T_{in}) in keV, (c) inner disc radius (R_{in}) in km, (d) photon index (Γ), and (e) equivalent width (EW) of iron Kα line in eV in Fig. 3. The grey points represent the spectral analysis result obtained with the Model-1 in all panels. Fig. 4 shows the variation of (a) 3−25 keV *AstroSat*/LAXPC count rate in count s^{-1}, (b) thermal disc flux (F_{DBB}) in 10^{-8} ergs cm^{-2} s^{-1}, (c) Comptonized power-law flux (F_{PL}) in 10^{-8} ergs cm^{-2} s^{-1}, (d) iron line flux (F_{Ga}) 10^{-8} ergs cm^{-2} s^{-1}, and (e) thermal emission fraction (f_{disc}).

From the spectral analysis with Model-1, we observed that N_H varied in the range of 0.7−0.8 × 10^{22} cm^{-2} during the observation duration. The T_{in} was found to fluctuate in the range of 0.9−1 keV until the *AstroSat* orbit 29 819 (MJD 59307.59). Then, the T_{in} decreased to ∼0.8 keV. The T_{in} was observed to be in the range of ∼0.7−0.8 keV for the rest of the observations. We also observed a variation in R_{in}. At the beginning of the observation, R_{in} was observed to be ∼32 km. Later, R_{in} was found to increase with R_{in} ∼ 40−45 km, indicating that the disc is moving outward.

At the beginning of the observations, the photon index Γ is found to be ∼2. Later, it decreased to Γ ∼1.8, as the source count rate decreased. The EW of the iron emission line was found to decrease as
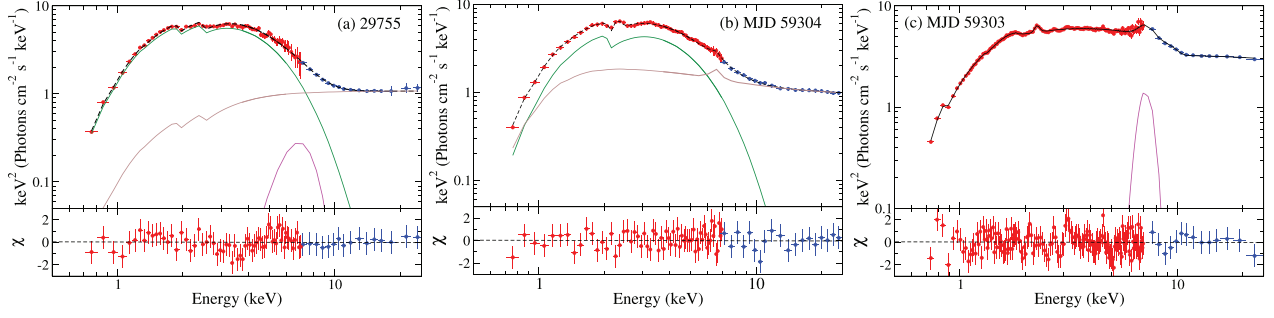
Figure 2. *Left panel*: Representative spectrum of GX 339–4 for orbit number 29 755 (MJD 59303.12), fitted with Model-1. The red and blue points represent the SXT and LAXPC data, respectively. The black dashed, grey solid, dark green solid, and magenta lines represent the total emission, Comptonized emission, disc-blackbody and iron line emission, respectively. *Middle panel*: Model-2 fitted spectrum for MJD 59304. The black dashed, grey solid and dark green solid lines represent the total emission, Comptonized and reprocessed emission, and disc-blackbody, respectively. *Right panel*: Spectrum for MJD 59303, fitted with Model-3. The black and magenta lines represent the total and iron line emission, respectively.
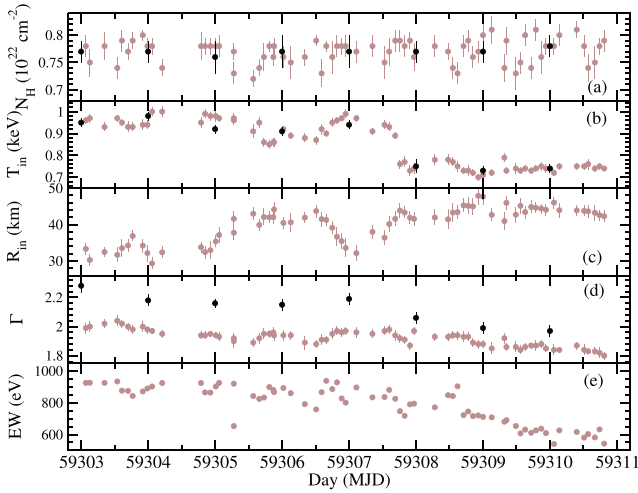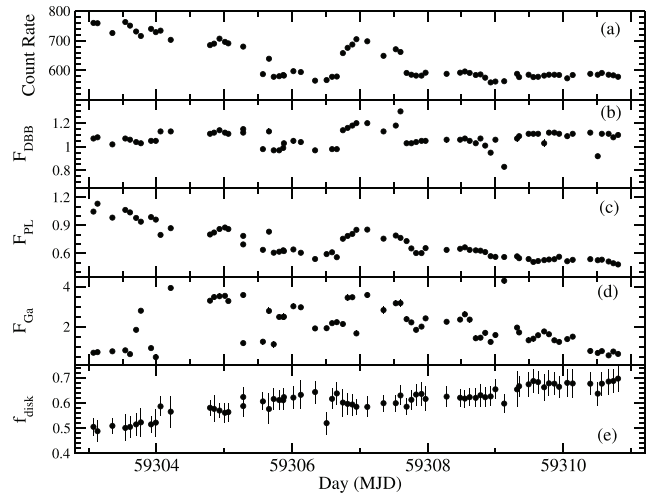

Figure 3. Variation of (a) line-of-sight equivalent hydrogen column density (N_H) in 10^{22} cm^{-2}, (b) inner disc temperature (T_{in}) in keV, (c) inner disc radius (R_{in}) in km, (d) photon index (Γ), and (e) equivalent width (EW) of Fe Kα line in eV are shown during our observation period. The black and grey points represent the result of one day-averaged and orbit wise spectral fitting with Model-2 and Model-1, respectively.

Figure 4. Evolution of (a) 3−25 keV *AstroSat*/LAXPC count rate in count s^{-1}, (b) thermal disc flux (F_{DBB}) in 10^{-8} ergs cm^{-2} s^{-1}, (c) Comptonized power-law flux (F_{PL}) in 10^{-8} ergs cm^{-2} s^{-1}, (d) iron line flux (F_{Ga}) in 10^{-10} ergs cm^{-2} s^{-1}, and (e) thermal emission fraction (f_{disc}) are shown during our observation period.

Γ decreased. The Pearson correlation between the Γ and EW is found to be $r = 0.84$ with p-value of $<10^{-3}$. Such a positive correlation for this source is consistent with the findings in the literature. As the disc is receding away from the BH in progressive orbits of *AstroSat* observation, the gravitational effects decrease. Therefore, the EW is decreasing. As the EW represents the reflection, the reflection strength decreases as the spectrum becomes hard. At the same time, we observed the fraction of the thermal emission (f_{disc}) increased towards the end of the observation period.

3.2.2 RELXILLLP

Next, we fitted the 1 d-averaged spectra in $0.7−25$ keV energy range with the physical RELXILLLP model, which replaces the NTHCOMP in the phenomenological model. The RELXILLLP model considers the lamp-post geometry. In this model, the corona is considered to be a point source, located at a height of 'h' from the BH. The hard X-ray photons from the corona are reprocessed in the disc and produce Fe K-line and reflection hump in the observed

spectrum. The complete model (hereafter Model-2) reads in XSPEC as TBABS∗(DISKBB + RELXILLLP). During the analysis, we kept the spin parameter frozen at 0.998, the inclination angle at 30º, and the outer disc radius at 400 R_g. As we could not constrain the cutoff energy, we also fixed it at 300 keV. The fitting with the RELXILLLP model gave us an acceptable fit (χ^2/dof $\sim$1) for all the 1 d-averaged spectra. The spectral analysis result is tabulated in Table B1.

From the day-wise spectral analysis with Model-2, we obtained a similar result as with Model-1. In Fig. 3, we show the variation of (a) line-of-sight hydrogen column density (N_H) in 10^{22} cm^{-2}, (b) inner disc temperature (T_{in}) in keV, and (d) photon index (Γ) obtained from Model-2 spectral fits with black points. During our observation period, the T_{in} is found to decrease from $\sim$1 to $\sim$0.7 keV. The Γ from the RELXILLLP model is somehow softer than the findings with the NTHCOMP model. This is because the RELXILLLP includes reprocessed emission, which is absent in the phenomenological model fitting. We found that the ionization parameter (ξ) and the iron abundances (A_{Fe}) remain same throughout the observation period, with log $\xi \sim 4$ and $A_{Fe} \sim 4 A_{\odot}$. The height of the corona is observed to change from $\sim$6.5 to $\sim$2 R_g during the observation period. The
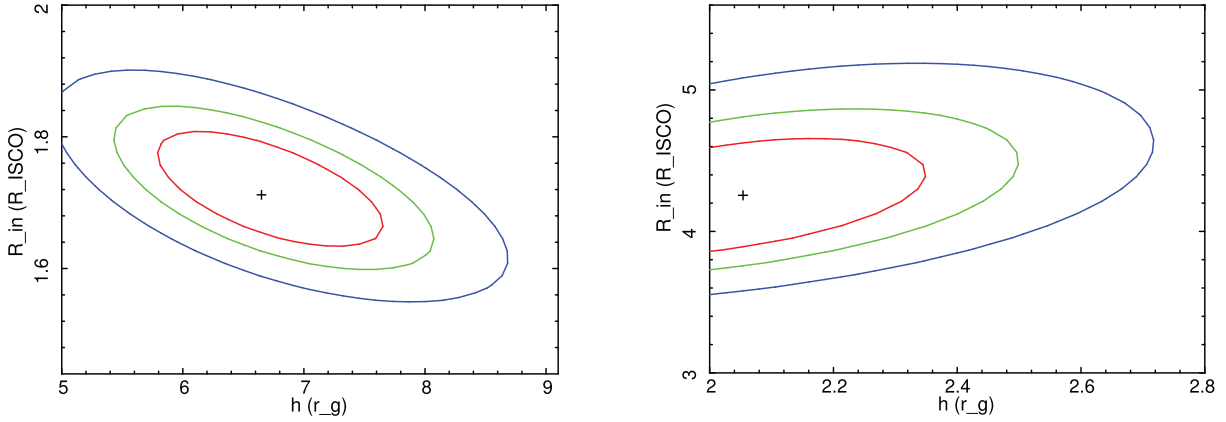
Figure 5. 2D-contours between the corona height (h) and inner disc radius (R_{in}) for the *AstroSat* observations on MJD 59 303 in the left panel, and for MJD 59 310 in the right panel.
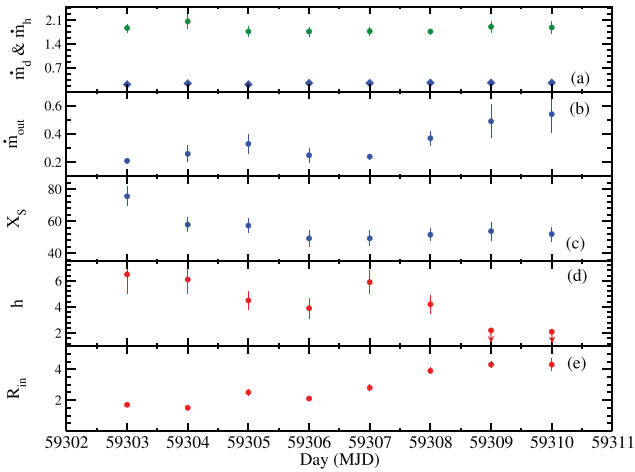
Figure 6. Evolution of (a) Keplerian disc accretion rate ($\dot{m}_d$ in $\dot{m}_{Edd}$; green) and sub-Keplerian flow rate ($\dot{m}_h$ in $\dot{m}_{Edd}$; blue), (b) mass outflow rate ($\dot{m}_{out}$ in $\dot{m}_{Edd}$) from Model-3, and (c) the size of the corona (X_s in R_g), (d) coronal height (h in R_g), and (e) inner disc radius (R_{in} in R_{ISCO}) from Model-2.

inner disc radius is found to increase from ∼1.7 to ∼4.3 R_{ISCO}, indicating a receding disc.

The middle panel of Fig. 2 shows the Model-2 fitted spectrum for MJD 59304. The black dashed, grey solid, and dark green solid lines represent the total emission, Comptonized and reprocessed emission (RELXILLLP) and disc-blackbody (DISKBB) emission, respectively. The variation of the spectral parameters obtained with Model-2 is shown with black points in Fig. 3. We show the variation of (a) the line-of-sight hydrogen column density (N_H) in 10^{22} cm^{-2}, (b) inner disc temperature (T_{in}) in keV, and (d) photon index (Γ). Fig. 5 shows the 2D-contours between the height of the corona (h) and the inner disc radius (R_{in}) for the *AstroSat* observations on MJD 59 303 and MJD 59 310 in the left and right panels, respectively. In Fig. 6, we show the variation of (d) coronal height (h in R_g) and (e) inner disc radius (R_{in} in R_{ISCO}) with MJDs with red points.

3.2.3 JETCAF

We also used physical model JETCAF, which includes jet/outflows (Mondal & Chakrabarti 2021) for further spectral analysis. In this

model, the accretion flow has two components: an optically thick, geometrically thin high viscous Keplerian flow on the equatorial plane submerged inside an optically thin, low viscous sub-Keplerian flow. The Keplerian flow produces the soft thermal multicolour disc blackbody emission. The sub-Keplerian flow forms an axis-symmetric shock which produces the dynamic corona at the post-shock region. The corona up-scatters the soft photons from the Keplerian flow and produces the hard power-law emission. The corona also acts as the base of the jet, i.e. the jet is launched from the corona (see Chakrabarti & Titarchuk 1995; Chakrabarti 1999, 2018; Mondal & Chakrabarti 2021, for details).

The JETACF model has six free parameters, such as the mass of the black hole (M_{BH}), the Keplerian disc accretion rate ($\dot{m}_d$ in Eddington rate $\dot{m}_{Edd}$), the sub-Keplerian halo rate ($\dot{m}_h$ in $\dot{m}_{Edd}$), the size of the corona or shock location (X_s in R_g), shock compression ratio (R, ratio of the matter density in post-shock to pre-shock region), and collimation factor of the jet/outflow ($f_{col} = \theta_{out}/\theta_{in}$; θ_{out} and θ_{in} are angle subtended by the outflow and inflow, respectively).

The JETCAF model does not contain the iron emission line. Hence, we added a Gaussian line at 6.4 keV to incorporate the iron line during the spectral analysis. The spectral model (hereafter Model-3) reads in XSPEC as TBABS∗(JETCAF+GAUSSIAN). We obtained an acceptable fit with the JETCAF model for all the 1 d-averaged spectra. The $\dot{m}_d$ and $\dot{m}_h$ varied in the range of ∼1.7−2.1 and ∼0.2−0.3 $\dot{m}_{Edd}$, respectively. The size of the corona was ∼75 R_g at the beginning of the outburst, and then it decreased to ∼50 R_g.

We also calculated the mass outflow rate ($\dot{m}_{out}$) from the R and f_{col}. The ratio of outflow to inflow rate is given by $R_{\dot{m}} = f_{col} f_0^{3/2} \frac{R}{4} \exp[\frac{3}{2} - f_0]$, where $f_0 = R^2/(R - 1$; Chakrabarti 1999). We found that $\dot{m}_{out}$ increased to 0.33 ± 0.07 $\dot{m}_{Edd}$ on MJD 59305, from 0.21 ± 0.02 $\dot{m}_{Edd}$ on MJD 59303. Later, it decreased briefly, and then $\dot{m}_{out}$ increased to 0.54 ± 0.13 $\dot{m}_{Edd}$ on MJD 59310.

From the spectral modelling with Model-3, we obtained the mass of the BH as 7.3 ± 0.6 $M_\odot$. The model normalization is also found to be constant across all the observations at $N = 11.5 \pm 1.5$, as expected from theoretical point-of-view. In the right panel of Fig. 2, we show the Model-3 fitted spectrum for MJD 59303. The black and magenta lines represent the total and iron emission line (GAUSSIAN), respectively. In Fig. 6, we show the variation of (a) Keplerian disc accretion rate ($\dot{m}_d$ in $\dot{m}_{Edd}$) and sub-Keplerian flow rate ($\dot{m}_h$ in $\dot{m}_{Edd}$), (b) mass outflow rate ($\dot{m}_{out}$ in $\dot{m}_{Edd}$), and (c) size of the corona (X_s in R_g). The spectral analysis result is tabulated in Table B2.

4 DISCUSSION

We studied the spectral and timing properties of GX 339-4 in $0.7-25$ keV energy range, using *AstroSat* observations during its 2021 outburst. *AstroSat* observations were carried in the rising phase of the outburst when the source was in the intermediate state. We used LAXPC data in $3-25$ keV range for the timing study, while we used combined SXT and LAXPC data in $0.7-25$ keV range for the spectral study.

4.1 Comparison between different spectral models

During our spectral analysis, we obtained N_H in the range of $\sim 0.7-0.8 \times 10^{22}$ cm^{-2} from all the models. Our estimated value of N_H is greater than the values reported in earlier studies, where N_H was found to be $\sim 0.5-0.6 \times 10^{22}$ cm^{-2} (Motta, Belloni & Homan 2009). In the previous studies, the abundances were considered to be AGNR (Anders & Grevesse 1989), whereas we considered WILMS abundances in this work. We fitted the data considering ANGR abundances, where we found that N_H varied in the range of $\sim 0.5-0.6 \times 10^{22}$ cm^{-2}.

We found a softer Γ while fitting the data with Model-2, compared to the Model-1. From the Model-1 fitting, the Γ varied in the range of $\Gamma \sim 1.8-2$, while in the case of the Model-2 fitting, Γ was found to be in the range of $2-2.3$. As the reprocessed emission is not included in Model-1, we obtained a somehow harder Γ. Another possibility for different Γ is using different primary continuum models in Model-1 and Model-2. In Model-1, NTHCOMP is used as the primary continuum, while CUTOFFPL is used in Model-2 as the continuum model. The NTHCOMP and CUTOFFPL treat the low-energy part of the spectrum differently, which may result in different Γ (e.g. Jana et al. 2021). However, the difference will not be large as the Γ is calculated from the high-energy part of the spectrum. We tested this by replacing NTHCOMP with CUTOFFPL in Model-1, and RELXILLLPCP with RELXILLLP in Model-2, and we found $\Delta\Gamma \sim 0.01 \pm 0.02$, in both the cases. Nonetheless, a different Γ is obtained from both models, the variation of the Γ is similar. The inner disc temperature (T_{in}) is obtained from both Model-1 and Model-2. We obtained a similar variation of the T_{in} from both models. At the beginning of the *AstroSat* observation, the T_{in} was ~ 1 keV. Later, the T_{in} decreased to ~ 0.7 keV.

We calculated the inner disc radius (R_{in}) from the DISKBB normalization in Model-1. We observed that R_{in} increased from ~ 30 to ~ 45 km during the observation period. The spectral analysis with Model-2 found that the R_{in} increased from ~ 1.7 to $\sim 4.3 R_{ISCO}$ during the observation period. The DISKBB yields somehow a higher value of R_{in} compared to the RELXILLLP model. This is because the DISKBB does not consider the spin of the black hole. Nonetheless, both models indicated a receding disc.

We obtained the coronal properties from Model-2 and Model-3. In Model-2, the RELXILLLP considers a lamp-post geometry, with the point source located at a distance of 'h' from the BH. We observed that 'h' decreased from ~ 7 to $\sim 2 R_g$ during the observation period, implying a contracting corona. On the other hand, in Model-3, JETCAF considers an extended corona, with the disc truncated at the boundary of the corona. The spectral analysis with Model-3 revealed a contracting corona with its size decreasing from ~ 75 to $\sim 50 R_g$ during the *AstroSat* observation period. As the RELXILLLP and JETCAF models consider different geometries of the corona, we obtained different sizes of the corona. However, both models suggested a contracting corona.
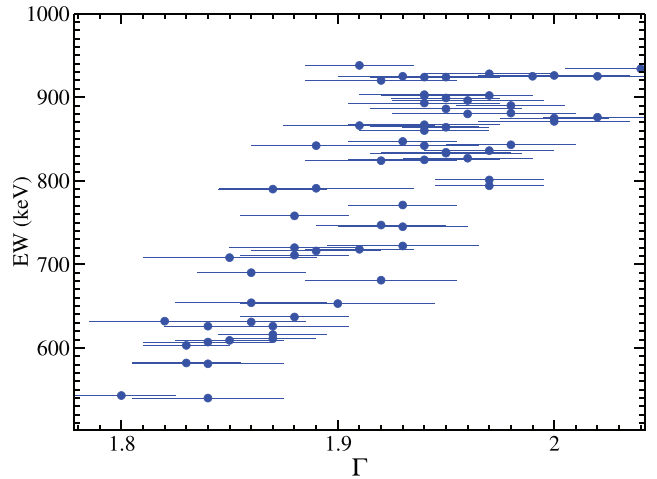
Figure 7. Variation of equivalent width (EW) of Fe Kα line as a function of power-law photon index (Γ).

4.2 Evolution of the inner accretion flow

At the beginning of the outburst, the LHS is observed, with the accretion disc truncated at a larger distance. In this state, the Comptonized emission dominates the spectrum with $f_{disc} < 20$ per cent (e.g. Remillard & McClintock 2006). As the outburst progresses, the disc emission starts to dominate, with the disc moving inward and the size of the Compton corona shrinking. The source moves to the HSS via IMS. The source enters the declining phase when the viscosity is turned off. As a result, the matter supply is cut-off, and the source moves to the quiescent state via IMS and LHS. In the IMS, a blobby jet or discrete ejection is observed. The Compton corona acts as the base of the jet. As a blob moves away at a relativistic speed, suddenly, a void is created at the Compton corona. The disc moves quickly to fill the void making the spectrum soft for a short time. As the corona recovers, the spectrum becomes harder. As a result, we observed fluctuations in the X-ray flux, T_{in}, and Γ in a very short time-scale in the IMS.

At the beginning of the *AstroSat* observation, GX 339–4 was in the SIMS, with $T_{in} \sim 1$ keV, and $\Gamma \sim 2.3$. The source moved to the HIMS at the end of the observation period. The source showed an AFP around MJD 59305–59306 as the X-ray flux decreased. The disc slowly moved outward as T_{in} decreased to ~ 0.7 keV. The spectrum became hard with decreasing Γ. In this case, one would expect f_{disc} to decrease. However, we observed an opposite scenario, where f_{disc} increases with a decrease in Γ. This is observed as F_{PL} is reduced, although F_{DBB} remains the same. During the observation period, the $\dot{m}_d$ was constant within uncertainty, which is responsible for a constant F_{DBB}.

The AFP can be explained in terms of an episodic ejection, which is observed in the IMS. If a blobby jet is produced, a part of the matter from the corona is ejected, leaving the size of the corona shrinking, which in turn, reduces F_{PL}, resulting in an AFP. At the same time, as the size of the corona decreases, the number of intercepted soft photons decreases, leading to inefficient cooling, which leads to the harder spectrum, i.e. decreasing Γ. Similar behaviour is also observed in other BHXBs (Vadawale et al. 2001, and references therein).

Above mentioned scenario is observed in GX 339–4. Initially, the coronal size was $\sim 75 R_g$ with mass ejection rate as $\sim 0.2 \dot{m}_{Edd}$ on MJD 59303. The jet flux was estimated to increase on MJD 59 305 with $\dot{m}_{out} \sim 0.33 \dot{m}_{Edd}$, indicating a huge amount of the mass ejection on that day. As a result, the corona size decreased to $\sim 50 R_g$ on the
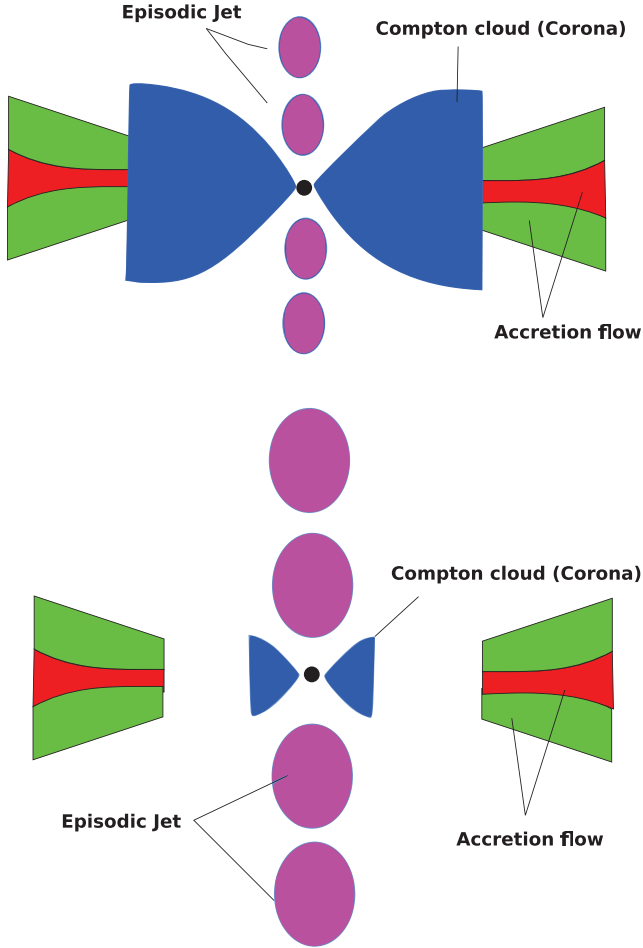
Figure 8. Cartoon diagram representing the accretion geometry in GX 339–4. A more extensive corona with episodic jet ejection is shown in the top panel, whereas the bottom panel shows a shrunk corona due to increased mass ejection rate. In both panels, the corona is represented in blue shaded region, whereas the magenta-coloured blobs represent the episodic jet. The sub-Keplerian and Keplerian accretion flows are represented with red- and green-coloured regions, respectively.

next day, on MJD 59306. After that, the corona remains at $\sim$50 R_g, with the mass ejection rate increased to $\sim$0.5 $\dot{m}_\text{out}$ at the end of our observation period. As more mass is ejected, the corona becomes weak with decreasing Comptonized flux. Fig. 8 shows the cartoon diagram of the inner accretion flow in GX 339–4. The top panel shows a larger corona with episodic jet ejection. With the increase in the mass ejection rate, the mass from the corona is ejected, leaving behind a shrunken corona.

Liu et al. (2022) studied the source on MJD 59303–59305 with *Insight-HXMT*, and suggested that the AFP is seen due to the change in the coronal power in a short time-scale. The authors suggested that there was a sudden change in the magnetic field, which led to a sudden heating effect in the corona, which reduced the coronal power. The authors did not find any variation in the coronal geometry, which contradicts our findings. The authors assumed a constant inner disc radius throughout their observation and found no variation of the coronal height (see table 2 of Liu et al. 2022). However, in our analysis, we allowed the inner disc radius to vary and found both R_in and h vary, indicating a dynamic inner accretion region.

Although, Peirano et al. (2023) did not study the AFP period, they suggested the existence of dual corona: a small compact corona

($\sim$25 R_g) with high feedback and an extended corona ($\sim$1500 R_g) with no feedback. Yang et al. (2023) argued that the extended corona could be the base of the jet and can explain the variation of type-B QPO. However, the QPOs can also be explained by a single corona model (Mondal et al. 2023). If the dual corona existed in GX 339–4, the outer corona could be ejected, leaving a smaller compact inner corona, which also supports our explanation of AFP.

4.3 Reprocessed emission

The reprocessed emission produced a Compton hump at $\sim$20−40 keV and a Fe Kα line at 6.4 keV. As we carried out our spectral analysis up to 25 keV, the Compton hump was not observed in the spectra. However, the Fe Kα line was detected at 6.4 keV while fitting the orbit-wise spectra with Model-1. We used the EW of the Fe Kα line to study the reprocessed emission in the source. Fig. 7 shows the variation of the EW as a function of Γ. We observed that the EW is correlated with Γ. This indicates that the reflection becomes stronger when the disc moves inward. This enables more hard photons to intercept the disc, resulting in increasing reprocessed emission, thereby, the EW. However, in the HSS, the coronal emission decreases, leading to a decrease in the reprocessed emission, i.e. EW. Generally, the EW is observed to correlate with the photon index up to $\Gamma \sim 2$ while the reprocessed emission saturates at $\Gamma > 2$; and decreases with further increasing Γ (e.g. Jana 2022, and references therein). A similar variation of the reflection is also observed in several active galactic nuclei and other BHXBs (Gilfanov, Churazov & Revnivtsev 1999; Zdziarski, Lubiński & Smith 1999; Lubiński & Zdziarski 2001; Ezhikode et al. 2020).

We used the relativistic reflection model RELXILLLP to analyse 1 d-averaged spectra. The reflection fraction (R_f) is not a free parameter in RELXILLLP, as it is estimated self-consistently. Hence, we estimated the flux of the reprocessed emission (F_ref) and primary emission (F_PL) in 10−25 keV to compute the reflection fraction ($R_\text{f} = F_\text{ref}/F_\text{PL}$). We found that the R_f decreases as the outburst progressed, following the similar variation of the EW of iron Kα line. The reprocessed emission generally depends on the disc ionization and hard X-ray emission. As disc ionization was constant during the observation period at $\log \xi \sim 10^4$ erg cm s^{-1}, the hard coronal X-ray is responsible for the change in the reprocessed emission. The decreasing F_PL naturally explains the decreasing the R_f, and EW.

5 SUMMARY

We studied spectral properties of the black hole binary GX 339–4 using *AstroSat* observations in 0.7−25 keV energy ranges during its 2021 outburst. Our key findings are given below.

(i) The 2021 outburst of GX 339–4 lasted for about 10 months. *AstroSat* observed the source in the intermediate state during the rising phase of the outburst.

(ii) The mass of BH is estimated to be 7.3 ± 0.6 M$_\odot$.

(iii) An 'alternate flux profile' was seen during our observation period, which can be explained with an episodic jet ejection.

(iv) The mass ejection rate was found to reach the peak when AFP was observed. As more mass is ejected, the corona becomes weak with decreasing Comptonized flux.

(v) During our observation period, we observed a dynamic inner accretion flow, with a contracting corona, and a receding disc.

(vi) A broad iron Kα line was observed in the spectrum. The EW of the iron line is found to correlate with the photon index Γ.

The reflection fraction is found to decrease with the decrease in the Comptonized flux.

(vii) The disc did not follow the $F_{DBB} - T_{in}^4$ relation during the *AstroSat* observation of the source, which is an indication of a moving disc.

DATA AVAILABILITY

We used the data of *AstroSat* observatories for this work.

REFERENCES

Agrawal P. C., 2006, Adv. Space Res., 38, 2989
Anders E., Grevesse N., 1989, Geochim. Cosmochim. Acta, 53, 197
Antia H. M. et al., 2017, ApJS, 231, 10
Antia H. M. et al., 2021, J. Astrophys. Astron., 42, 32
Arnaud K. A., 1996, in Jacoby G. H., Barnes J.eds, ASP Conf. Ser. Vol. 101, Astronomical Data Analysis Software and Systems V. Astron. Soc. Pac., San Francisco, p. 17
Bachetti M. et al., 2015, ApJ, 800, 109
Basak R., Zdziarski A. A., 2016, MNRAS, 458, 2199
Chakrabarti S. K., 1999, A&A, 351, 185
Chakrabarti S. K., 2018, in Bianchi M., Jansen R. T., Ruffini R.eds, Fourteenth Marcel Grossmann Meeting on Recent Developments in Theoretical and Experimental General Relativity, Astrophysics, and Relativistic Field Theories, World Scientific Publishing, Singapore, p.369,
Chakrabarti S., Titarchuk L. G., 1995, ApJ, 455, 623
Corbel S., Tzioumis T., Tremou L., Carotenuto F., 2021, Astron. Telegram, 14953, 1
Cowley A. P., Schmidtke P. C., Hutchings J. B., Crampton D., 2002, AJ, 123, 1741
Dauser T., García J., Walton D. J., Eikmann W., Kallman T., McClintock J., Wilms J., 2016, A&A, 590, A76
Debnath D., Mondal S., Chakrabarti S. K., 2015, MNRAS, 447, 1984
Dinçer T., Kalemci E., Buxton M. M., Bailyn C. D., Tomsick J. A., Corbel S., 2012, ApJ, 753, 55
Done C., Gierliński M., Kubota A., 2007, A&A Rev., 15, 1
Ezhikode S. H., Dewangan G. C., Misra R., Philip N. S., 2020, MNRAS, 495, 3373
Fabian A. C., Rees M. J., Stella L., White N. E., 1989, MNRAS, 238, 729
Fender R., Belloni T., 2004, ARA&A, 42, 317
Ferrigno C., Grinberg V., Bozzo E., Savchenko V., Ducci L., Wilms J., Thalhammer P., Rodriguez J., 2021, Astron. Telegram, 14440, 1
García J., Dauser T., Reynolds C. S., Kallman T. R., McClintock J. E., Wilms J., Eikmann W., 2013, ApJ, 768, 146
Garcia J., Tomsick J., Harrison F., Connors R., Mastroserio G., 2021, Astron. Telegram, 14352, 1
Gardner E., Done C., 2013, MNRAS, 434, 3454
Gilfanov M., Churazov E., Revnivtsev M., 1999, A&A, 352, 182
Haardt F., Maraschi L., 1993, ApJ, 413, 507
Husain N., Mudambi S. P., Garg A., Misra R., Sen S., Maqbool B., 2021, Astron. Telegram, 14400, 1
Jana A., 2022, MNRAS, 517, 3588
Jana A., Jaisawal G. K., Naik S., Kumari N., Chhotaray B., Altamirano D., Remillard R. A., Gendreau K. C., 2021, MNRAS, 504, 4793
Jana A., Naik S., Jaisawal G. K., Chhotaray B., Kumari N., Gupta S., 2022, MNRAS, 511, 3922
Kubota A., Tanaka Y., Makishima K., Ueda Y., Dotani T., Inoue H., Yamaoka K., 1998, PASJ, 50, 667
Liu H., Zhang L., Tao L., Chen Y., Qu J., Zhang S., Zhang S.-n., 2021, Astron. Telegram, 14504, 1
Liu H., Jiang J., Zhang Z., Bambi C., Ji L., Kong L., Zhang S., 2022, MNRAS, 513, 4308
Lubiński P., Zdziarski A. A., 2001, MNRAS, 323, L37
Makishima K., Maejima Y., Mitsuda K., Bradt H. V., Remillard R. A., Tuohy I. R., Hoshi R., Nakagawa M., 1986, ApJ, 308, 635
Markert T. H., Canizares C. R., Clark G. W., Lewin W. H. G., Schnopper H. W., Sprott G. F., 1973, ApJ, 184, L67
Matt G., Perola G. C., Piro L., 1991, A&A, 247, 25
Miller J. M. et al., 2008, ApJ, 679, L113
Mitsuda K. et al., 1984, PASJ, 36, 741
Mondal S., Adhikari T. P., Singh C. B., 2021, MNRAS, 505, 1071
Mondal S., Chakrabarti S. K., 2021, ApJ, 920, 41
Mondal S., Chakrabarti S. K., Debnath D., 2016, Ap&SS, 361, 309
Mondal S., Salgundi A., Chatterjee D., Jana A., Chang H. K., Naik S., 2023, MNRAS, 526, 4718
Motta S., Belloni T., Homan J., 2009, MNRAS, 400, 1603
Nandi A., Chakrabarti S. K., Vadawale S. V., Rao A. R., 2001, A&A, 380, 245
Nandi A., Debnath D., Mandal S., Chakrabarti S. K., 2012, A&A, 542, A56
Pal S., Mandal M., Hazra M., Saha D., Ghanta A., 2021, Astron. Telegram, 14351, 1
Parker M. L. et al., 2016, ApJ, 821, L6
Peirano V., Méndez M., García F., Belloni T., 2023, MNRAS, 519, 1336
Plant D. S., Fender R. P., Ponti G., Muñoz-Darias T., Coriat M., 2014, MNRAS, 442, 1767
Ramadevi M. C. et al., 2018, J. Astrophys. Astron., 39, 11
Rao A. R., Bhattacharya D., Bhalerao V. B., Vadawale S. V., Sreekumar S., 2017, Curr. Sci., 113, 595
Reis R. C., Fabian A. C., Ross R. R., Miniutti G., Miller J. M., Reynolds C., 2008, MNRAS, 387, 1489
Remillard R. A., McClintock J. E., 2006, ARA&A, 44, 49
Saikia P., Baglio M. C., Russell D. M., Bramich D. M., Caruso E., Lewis F., 2021, Astron. Telegram, 14419, 1
Shakura N. I., Sunyaev R. A., 1973, A&A, 500, 33
Shimura T., Takahara F., 1995, ApJ, 445, 780
Singh K. P. et al., 2017, J. Astrophys. Astron., 38, 29
Sreehari H., Iyer N., Radhika D., Nandi A., Mandal S., 2019, Adv. Space Res., 63, 1374
Stiele H., Kong A. K. H., 2023, MNRAS, 522, 268
Sunyaev R. A., Titarchuk L. G., 1980, A&A, 500, 167
Sunyaev R. A., Titarchuk L. G., 1985, A&A, 143, 374
Tandon S. N. et al., 2017, AJ, 154, 128
Tomsick J. A., Yamaoka K., Corbel S., Kaaret P., Kalemci E., Migliari S., 2009, ApJ, 707, L87
Vadawale S. V., Rao A. R., Nandi A., Chakrabarti S. K., 2001, A&A, 370, L17
Verner D. A., Ferland G. J., Korista K. T., Yakovlev D. G., 1996, ApJ, 465, 487
Wang J. et al., 2021, Astron. Telegram, 14384, 1
Wilms J., Allen A., McCray R., 2000, ApJ, 542, 914
Yang Q.-X., Xie F.-G., Yuan F., Zdziarski A. A., Gierliński M., Ho L. C., Yu Z., 2015, MNRAS, 447, 1692
Yang Z.-X. et al., 2023, MNRAS, 521, 3570
Zdziarski A. A., Johnson W. N., Magdziarz P., 1996, MNRAS, 283, 193

Zdziarski A. A., Lubiński P., Smith D. A., 1999, MNRAS, 303, L11
Zdziarski A. A., Ziółkowski J., Mikołajewska J., 2019, MNRAS, 488, 1026
Zycki P. T., Czerny B., 1994, MNRAS, 266, 653
Życki P. T., Done C., Smith D. A., 1999, MNRAS, 309, 561

APPENDIX A: TABLE A

Table A1. Best-fitting parameters obtained from the spectral fitting of data obtained from the combined SXT and LAXPC observations in the 0.7−25 keV energy range.

Orbit	Avg. MJD	N_H $(10^{22}$ cm$^{-2})$	T_{in} (keV)	R_{in} (km)	Γ	EW (eV)	χ^2/dof	F_{tot} $(10^{-8}$ erg cm s$^{-1})$	f_{disc}
29750	59303.06	$0.78^{+0.02}_{-0.02}$	$0.96^{+0.02}_{-0.01}$	$33.34^{+1.43}_{-1.60}$	$1.99^{+0.04}_{-0.03}$	925^{+28}_{-33}	617/639	2.12 ± 0.02	0.50 ± 0.01
29755	59303.12	$0.75^{+0.02}_{-0.03}$	$0.97^{+0.02}_{-0.02}$	$30.31^{+1.48}_{-1.64}$	$2.00^{+0.02}_{-0.05}$	926^{+25}_{-35}	617/639	2.22 ± 0.02	0.49 ± 0.01
29756	59303.34	$0.78^{+0.03}_{-0.02}$	$0.93^{+0.02}_{-0.02}$	$32.46^{+1.22}_{-1.38}$	$2.02^{+0.02}_{-0.04}$	925^{+20}_{-26}	569/636	2.01 ± 0.02	0.52 ± 0.01
29758	59303.54	$0.74^{+0.03}_{-0.01}$	$0.97^{+0.01}_{-0.02}$	$31.70^{+2.06}_{-1.78}$	$2.04^{+0.04}_{-0.03}$	934^{+17}_{-21}	594/639	2.14 ± 0.02	0.50 ± 0.01
29759	59303.61	$0.79^{+0.02}_{-0.02}$	$0.95^{+0.02}_{-0.01}$	$33.53^{+2.24}_{-2.50}$	$2.02^{+0.02}_{-0.02}$	876^{+21}_{-26}	589/639	2.10 ± 0.02	0.50 ± 0.01
29760	59303.69	$0.77^{+0.01}_{-0.02}$	$0.93^{+0.03}_{-0.02}$	$34.25^{+1.99}_{-1.48}$	$2.00^{+0.03}_{-0.02}$	875^{+16}_{-19}	690/638	2.04 ± 0.02	0.51 ± 0.02
29761	59303.77	$0.79^{+0.02}_{-0.01}$	$0.93^{+0.02}_{-0.02}$	$36.86^{+1.69}_{-1.24}$	$1.98^{+0.02}_{-0.04}$	843^{+19}_{-25}	607/638	2.00 ± 0.02	0.51 ± 0.02
29763	59303.91	$0.80^{+0.01}_{-0.01}$	$0.94^{+0.02}_{-0.03}$	$34.23^{+1.65}_{-1.98}$	$2.00^{+0.04}_{-0.03}$	871^{+22}_{-33}	657/639	2.04 ± 0.02	0.51 ± 0.01
29764	59303.49	$0.78^{+0.02}_{-0.01}$	$0.94^{+0.02}_{-0.02}$	$32.17^{+2.15}_{-2.33}$	$1.98^{+0.02}_{-0.03}$	890^{+18}_{-17}	686/639	2.01 ± 0.02	0.52 ± 0.02
29765	59304.05	$0.78^{+0.01}_{-0.02}$	$1.00^{+0.02}_{-0.02}$	$29.34^{+1.40}_{-1.62}$	$1.97^{+0.02}_{-0.03}$	902^{+20}_{-24}	661/638	1.99 ± 0.01	0.57 ± 0.01
29770	59304.20	$0.74^{+0.02}_{-0.01}$	$1.00^{+0.03}_{-0.02}$	$32.40^{+1.33}_{-1.71}$	$1.95^{+0.02}_{-0.02}$	924^{+23}_{-28}	665/635	2.04 ± 0.02	0.55 ± 0.02
29776	59304.78	$0.78^{+0.02}_{-0.03}$	$0.95^{+0.02}_{-0.03}$	$33.79^{+1.30}_{-1.66}$	$1.94^{+0.02}_{-0.03}$	924^{+28}_{-35}	604/639	1.94 ± 0.02	0.57 ± 0.02
29777	59304.85	$0.78^{+0.01}_{-0.02}$	$0.99^{+0.02}_{-0.02}$	$32.44^{+1.56}_{-1.96}$	$1.94^{+0.03}_{-0.03}$	865^{+43}_{-49}	679/637	1.98 ± 0.02	0.56 ± 0.02
29778	59304.93	$0.78^{+0.02}_{-0.01}$	$0.98^{+0.03}_{-0.01}$	$32.95^{+2.23}_{-2.48}$	$1.95^{+0.02}_{-0.02}$	864^{+35}_{-48}	621/638	2.03 ± 0.02	0.56 ± 0.02
29779	59304.50	$0.78^{+0.01}_{-0.02}$	$0.98^{+0.03}_{-0.02}$	$35.39^{+1.92}_{-1.37}$	$1.94^{+0.01}_{-0.03}$	902^{+28}_{-41}	672/638	2.03 ± 0.02	0.55 ± 0.02
29784	59305.05	$0.78^{+0.01}_{-0.03}$	$0.97^{+0.02}_{-0.01}$	$37.14^{+2.03}_{-2.29}$	$1.93^{+0.02}_{-0.04}$	925^{+26}_{-36}	661/638	2.00 ± 0.01	0.55 ± 0.01
29785	59305.27	$0.77^{+0.02}_{-0.01}$	$0.97^{+0.02}_{-0.03}$	$37.75^{+2.13}_{-1.69}$	$1.92^{+0.04}_{-0.03}$	920^{+45}_{-52}	662/639	1.94 ± 0.02	0.57 ± 0.02
29787	59305.28	$0.73^{+0.02}_{-0.02}$	$0.96^{+0.02}_{-0.02}$	$41.58^{+2.00}_{-2.16}$	$1.90^{+0.04}_{-0.05}$	653^{+23}_{-28}	698/639	1.86 ± 0.02	0.62 ± 0.02
29788	59305.57	$0.72^{+0.02}_{-0.02}$	$0.91^{+0.03}_{-0.03}$	$42.98^{+1.50}_{-1.83}$	$1.89^{+0.03}_{-0.03}$	842^{+19}_{-25}	664/638	1.63 ± 0.01	0.60 ± 0.02
29789	59305.66	$0.74^{+0.01}_{-0.02}$	$0.95^{+0.03}_{-0.02}$	$39.88^{+1.37}_{-1.67}$	$1.92^{+0.03}_{-0.03}$	824^{+42}_{-53}	625/638	1.99 ± 0.03	0.57 ± 0.02
29790	59305.73	$0.76^{+0.02}_{-0.03}$	$0.86^{+0.02}_{-0.02}$	$42.08^{+2.50}_{-2.03}$	$1.95^{+0.04}_{-0.03}$	833^{+37}_{-45}	628/639	1.59 ± 0.02	0.61 ± 0.03
29791	59305.80	$0.78^{+0.01}_{-0.01}$	$0.85^{+0.03}_{-0.01}$	$42.00^{+1.59}_{-1.69}$	$1.95^{+0.02}_{-0.03}$	899^{+41}_{-48}	674/639	1.61 ± 0.01	0.60 ± 0.01
29792	59305.86	$0.76^{+0.01}_{-0.02}$	$0.86^{+0.02}_{-0.02}$	$42.03^{+1.66}_{-2.07}$	$1.96^{+0.03}_{-0.04}$	880^{+33}_{-39}	639/639	1.64 ± 0.01	0.60 ± 0.02
29793	59305.88	$0.78^{+0.01}_{-0.02}$	$0.86^{+0.02}_{-0.02}$	$44.17^{+1.91}_{-2.19}$	$1.94^{+0.03}_{-0.04}$	867^{+47}_{-58}	667/639	1.67 ± 0.02	0.61 ± 0.02
29794	59305.51	$0.76^{+0.02}_{-0.02}$	$0.92^{+0.02}_{-0.01}$	$40.46^{+1.52}_{-1.67}$	$1.94^{+0.03}_{-0.04}$	893^{+41}_{-46}	624/639	1.72 ± 0.03	0.61 ± 0.02
29799	59306.13	$0.75^{+0.03}_{-0.03}$	$0.89^{+0.01}_{-0.02}$	$40.62^{+2.52}_{-2.67}$	$1.94^{+0.03}_{-0.03}$	860^{+18}_{-22}	648/639	1.67 ± 0.02	0.62 ± 0.03
29801	59306.34	$0.76^{+0.01}_{-0.02}$	$0.88^{+0.03}_{-0.01}$	$41.93^{+1.37}_{-1.58}$	$1.89^{+0.04}_{-0.05}$	791^{+25}_{-29}	657/633	1.52 ± 0.03	0.63 ± 0.03
29802	59306.51	$0.79^{+0.01}_{-0.01}$	$0.87^{+0.02}_{-0.02}$	$43.73^{+1.95}_{-1.58}$	$1.88^{+0.03}_{-0.02}$	758^{+28}_{-37}	673/635	1.25 ± 0.02	0.51 ± 0.02
29803	59306.58	$0.73^{+0.02}_{-0.03}$	$0.92^{+0.03}_{-0.02}$	$41.48^{+2.11}_{-1.73}$	$1.91^{+0.04}_{-0.03}$	866^{+24}_{-30}	701/639	1.61 ± 0.02	0.61 ± 0.02
29804	59306.65	$0.78^{+0.01}_{-0.01}$	$0.90^{+0.02}_{-0.01}$	$41.29^{+1.47}_{-1.67}$	$1.91^{+0.02}_{-0.02}$	938^{+18}_{-24}	622/638	1.56 ± 0.01	0.63 ± 0.01
29805	59306.74	$0.76^{+0.03}_{-0.03}$	$0.95^{+0.02}_{-0.02}$	$39.14^{+1.61}_{-1.90}$	$1.95^{+0.04}_{-0.04}$	886^{+21}_{-25}	626/639	1.92 ± 0.02	0.59 ± 0.01
29806	59306.82	$0.78^{+0.02}_{-0.02}$	$0.96^{+0.01}_{-0.02}$	$36.65^{+2.39}_{-2.69}$	$1.97^{+0.04}_{-0.02}$	928^{+27}_{-33}	622/638	1.98 ± 0.02	0.58 ± 0.01
29807	59306.89	$0.78^{+0.01}_{-0.01}$	$0.97^{+0.01}_{-0.01}$	$35.45^{+1.98}_{-2.24}$	$1.96^{+0.03}_{-0.04}$	827^{+33}_{-36}	708/638	2.02 ± 0.02	0.58 ± 0.02
29808	59306.94	$0.78^{+0.02}_{-0.02}$	$0.99^{+0.02}_{-0.02}$	$33.60^{+2.35}_{-2.69}$	$1.97^{+0.02}_{-0.03}$	801^{+39}_{-48}	619/639	2.06 ± 0.02	0.58 ± 0.02
29814	59306.61	$0.77^{+0.02}_{-0.02}$	$0.97^{+0.01}_{-0.02}$	$32.15^{+2.10}_{-2.20}$	$1.96^{+0.03}_{-0.04}$	896^{+15}_{-19}	681/639	2.09 ± 0.02	0.57 ± 0.02
29816	59307.35	$0.78^{+0.01}_{-0.03}$	$0.91^{+0.02}_{-0.01}$	$38.00^{+2.08}_{-1.57}$	$1.95^{+0.02}_{-0.03}$	834^{+25}_{-29}	626/639	1.91 ± 0.02	0.59 ± 0.02
29817	59307.53	$0.75^{+0.03}_{-0.03}$	$0.94^{+0.02}_{-0.02}$	$36.41^{+2.34}_{-1.75}$	$1.97^{+0.03}_{-0.03}$	836^{+23}_{-30}	629/646	2.00 ± 0.02	0.59 ± 0.02
29818	59307.60	$0.77^{+0.02}_{-0.03}$	$0.93^{+0.02}_{-0.02}$	$40.15^{+1.87}_{-2.33}$	$1.98^{+0.03}_{-0.03}$	881^{+22}_{-30}	626/639	2.10 ± 0.02	0.62 ± 0.01
29819	59307.69	$0.79^{+0.01}_{-0.03}$	$0.89^{+0.02}_{-0.01}$	$41.58^{+1.80}_{-2.12}$	$1.94^{+0.04}_{-0.03}$	825^{+32}_{-26}	612/646	1.78 ± 0.02	0.57 ± 0.02
29820	59307.76	$0.79^{+0.02}_{-0.02}$	$0.76^{+0.02}_{-0.02}$	$43.84^{+1.93}_{-2.11}$	$1.92^{+0.04}_{-0.03}$	747^{+38}_{-46}	681/638	1.70 ± 0.01	0.60 ± 0.01
29821	59307.83	$0.78^{+0.02}_{-0.02}$	$0.77^{+0.03}_{-0.02}$	$43.31^{+1.50}_{-1.59}$	$1.91^{+0.02}_{-0.03}$	718^{+40}_{-30}	700/638	1.66 ± 0.01	0.62 ± 0.02
29822	59307.90	$0.79^{+0.02}_{-0.01}$	$0.73^{+0.03}_{-0.02}$	$41.87^{+1.55}_{-1.75}$	$1.87^{+0.03}_{-0.02}$	790^{+39}_{-32}	693/646	1.67 ± 0.02	0.63 ± 0.02
29823	59307.47	$0.76^{+0.03}_{-0.02}$	$0.74^{+0.02}_{-0.03}$	$41.56^{+1.82}_{-1.84}$	$1.97^{+0.03}_{-0.02}$	794^{+38}_{-45}	691/643	1.73 ± 0.02	0.61 ± 0.02
29828	59307.81	$0.74^{+0.03}_{-0.02}$	$0.79^{+0.01}_{-0.02}$	$40.95^{+2.20}_{-2.47}$	$1.92^{+0.04}_{-0.03}$	681^{+45}_{-57}	696/639	1.65 ± 0.03	0.64 ± 0.03
29830	59308.27	$0.78^{+0.02}_{-0.02}$	$0.78^{+0.03}_{-0.02}$	$41.94^{+2.43}_{-1.88}$	$1.93^{+0.02}_{-0.03}$	771^{+29}_{-31}	670/639	1.72 ± 0.03	0.62 ± 0.03

Table A1. *continued* Best-fitting parameters obtained from the spectral fitting of data obtained from the combined SXT and LAXPC observations in the $0.7-25$ keV energy range.

Orbit	Avg. MJD	N_H $(10^{22}$ cm$^{-2})$	T_{in} (keV)	R_{in} (km)	Γ	EW (eV)	χ^2/dof	F_{tot} $(10^{-8}$ erg cm s$^{-1})$	f_{disc}
29831	59308.47	$0.77^{+0.01}_{-0.02}$	$0.78^{+0.02}_{-0.03}$	$41.44^{+2.60}_{-2.77}$	$1.93^{+0.03}_{-0.02}$	847^{+30}_{-25}	679/638	1.73 ± 0.02	0.61 ± 0.03
29832	59308.54	$0.74^{+0.03}_{-0.01}$	$0.77^{+0.02}_{-0.02}$	$43.29^{+2.83}_{-2.25}$	$1.94^{+0.03}_{-0.02}$	842^{+24}_{-31}	668/639	1.76 ± 0.02	0.61 ± 0.03
29833	59308.61	$0.73^{+0.02}_{-0.02}$	$0.75^{+0.03}_{-0.02}$	$43.43^{+1.67}_{-2.07}$	$1.94^{+0.04}_{-0.02}$	903^{+35}_{-27}	647/641	1.71 ± 0.02	0.61 ± 0.03
29834	59308.70	$0.78^{+0.01}_{-0.03}$	$0.73^{+0.02}_{-0.01}$	$45.26^{+1.65}_{-2.06}$	$1.93^{+0.03}_{-0.04}$	722^{+26}_{-35}	674/638	1.67 ± 0.02	0.61 ± 0.02
29835	59308.77	$0.79^{+0.02}_{-0.02}$	$0.73^{+0.03}_{-0.02}$	$45.15^{+2.03}_{-2.36}$	$1.93^{+0.04}_{-0.02}$	745^{+29}_{-41}	631/639	1.71 ± 0.02	0.62 ± 0.02
29836	59308.85	$0.76^{+0.02}_{-0.02}$	$0.72^{+0.02}_{-0.01}$	$44.96^{+2.18}_{-2.46}$	$1.89^{+0.03}_{-0.03}$	716^{+31}_{-38}	667/643	1.64 ± 0.03	0.61 ± 0.03
29837	59308.92	$0.77^{+0.02}_{-0.02}$	$0.70^{+0.02}_{-0.01}$	$47.90^{+2.23}_{-2.44}$	$1.88^{+0.04}_{-0.03}$	720^{+25}_{-30}	686/645	1.53 ± 0.02	0.62 ± 0.02
29838	59308.49	$0.80^{+0.02}_{-0.02}$	$0.71^{+0.01}_{-0.03}$	$47.66^{+2.14}_{-2.51}$	$1.88^{+0.02}_{-0.03}$	711^{+24}_{-32}	685/649	1.63 ± 0.03	0.65 ± 0.04
29843	59309.12	$0.81^{+0.02}_{-0.03}$	$0.72^{+0.01}_{-0.02}$	$42.68^{+1.58}_{-1.93}$	$1.85^{+0.04}_{-0.04}$	708^{+36}_{-46}	622/647	1.43 ± 0.03	0.58 ± 0.04
29845	59309.34	$0.79^{+0.03}_{-0.02}$	$0.73^{+0.02}_{-0.01}$	$45.99^{+1.65}_{-2.05}$	$1.86^{+0.03}_{-0.02}$	690^{+28}_{-32}	711/638	1.65 ± 0.02	0.66 ± 0.04
29846	59309.49	$0.73^{+0.03}_{-0.03}$	$0.74^{+0.03}_{-0.02}$	$42.71^{+1.86}_{-2.31}$	$1.86^{+0.04}_{-0.03}$	654^{+18}_{-23}	663/649	1.66 ± 0.02	0.67 ± 0.03
29847	59309.56	$0.75^{+0.02}_{-0.02}$	$0.73^{+0.02}_{-0.01}$	$45.15^{+1.80}_{-2.33}$	$1.84^{+0.04}_{-0.02}$	607^{+19}_{-28}	634/645	1.63 ± 0.02	0.68 ± 0.02
29848	59309.63	$0.80^{+0.02}_{-0.02}$	$0.74^{+0.01}_{-0.02}$	$43.43^{+1.43}_{-1.86}$	$1.86^{+0.02}_{-0.03}$	631^{+26}_{-36}	692/646	1.64 ± 0.02	0.67 ± 0.02
29849	59309.72	$0.74^{+0.03}_{-0.01}$	$0.73^{+0.02}_{-0.01}$	$44.85^{+1.48}_{-1.84}$	$1.87^{+0.02}_{-0.02}$	611^{+21}_{-29}	611/648	1.57 ± 0.04	0.65 ± 0.04
29850	59309.78	$0.81^{+0.02}_{-0.02}$	$0.74^{+0.02}_{-0.01}$	$44.62^{+1.35}_{-1.55}$	$1.87^{+0.03}_{-0.04}$	626^{+26}_{-21}	612/642	1.67 ± 0.03	0.67 ± 0.03
29851	59309.86	$0.76^{+0.03}_{-0.03}$	$0.75^{+0.03}_{-0.01}$	$44.40^{+1.35}_{-1.16}$	$1.88^{+0.03}_{-0.02}$	637^{+28}_{-35}	669/631	1.67 ± 0.02	0.67 ± 0.02
29852	59309.94	$0.78^{+0.02}_{-0.01}$	$0.74^{+0.02}_{-0.02}$	$44.09^{+1.56}_{-1.69}$	$1.85^{+0.02}_{-0.03}$	609^{+23}_{-26}	612/643	1.68 ± 0.02	0.66 ± 0.03
29857	59309.48	$0.78^{+0.02}_{-0.01}$	$0.72^{+0.02}_{-0.01}$	$46.02^{+1.68}_{-1.46}$	$1.84^{+0.03}_{-0.04}$	540^{+28}_{-39}	623/647	1.62 ± 0.02	0.67 ± 0.03
29859	59309.63	$0.80^{+0.02}_{-0.02}$	$0.75^{+0.01}_{-0.02}$	$43.92^{+1.84}_{-2.09}$	$1.84^{+0.02}_{-0.02}$	626^{+17}_{-23}	674/645	1.65 ± 0.02	0.67 ± 0.02
29860	59310.39	$0.81^{+0.01}_{-0.02}$	$0.75^{+0.01}_{-0.02}$	$43.89^{+1.34}_{-1.49}$	$1.87^{+0.02}_{-0.03}$	616^{+20}_{-28}	634/643	1.66 ± 0.02	0.67 ± 0.03
29861	59310.50	$0.78^{+0.02}_{-0.02}$	$0.75^{+0.02}_{-0.02}$	$43.77^{+1.28}_{-1.53}$	$1.84^{+0.04}_{-0.03}$	581^{+22}_{-25}	677/648	1.45 ± 0.03	0.63 ± 0.03
29862	59310.57	$0.74^{+0.03}_{-0.02}$	$0.76^{+0.02}_{-0.03}$	$43.63^{+1.64}_{-1.87}$	$1.83^{+0.02}_{-0.02}$	603^{+30}_{-37}	691/639	1.65 ± 0.02	0.67 ± 0.02
29863	59310.66	$0.75^{+0.03}_{-0.03}$	$0.74^{+0.01}_{-0.02}$	$43.25^{+1.97}_{-2.14}$	$1.83^{+0.02}_{-0.03}$	582^{+29}_{-36}	688/642	1.63 ± 0.02	0.68 ± 0.03
29864	59310.73	$0.78^{+0.02}_{-0.01}$	$0.75^{+0.02}_{-0.01}$	$42.58^{+1.44}_{-1.56}$	$1.82^{+0.03}_{-0.04}$	632^{+25}_{-32}	672/639	1.58 ± 0.02	0.68 ± 0.03
29865	59310.81	$0.79^{+0.02}_{-0.02}$	$0.74^{+0.01}_{-0.01}$	$42.27^{+1.52}_{-1.70}$	$1.80^{+0.02}_{-0.03}$	543^{+27}_{-31}	671/649	1.58 ± 0.03	0.69 ± 0.04

Note. Errors are quoted at 90 per cent confidence.

APPENDIX B: SPECTRA ANALYSIS RESULT OF 1 D-AVERAGED SPECTRA

Table B1. Best-fitting parameters obtained from the spectral fitting of 1 d-averaged data with RELXILLLP model.

Orbit	MJD	T_{in} (keV)	Γ	R_{in} (R_{ISCO})	h (R_g)	$\log \xi$ (erg cm s^{-1})	A_{Fe} $(A_\odot)$	R_f	χ^2/dof
29750–29764	59303	0.95 ± 0.02	2.28 ± 0.05	1.7 ± 0.1	$6.5^{+1.5}_{-0.8}$	3.9 ± 0.4	3.9 ± 0.3	1.27 ± 0.12	767/632
29765–29778	59304	0.98 ± 0.02	2.18 ± 0.04	1.5 ± 0.1	$6.1^{+2.2}_{-1.1}$	4.1 ± 0.4	4.1 ± 0.3	1.13 ± 0.15	687/632
29779–29793	59305	0.92 ± 0.02	2.16 ± 0.03	2.5 ± 0.2	$4.5^{+0.8}_{-0.7}$	3.9 ± 0.3	4.1 ± 0.3	1.04 ± 0.11	728/632
29794–29808	59306	0.91 ± 0.02	2.15 ± 0.04	2.1 ± 0.1	$3.9^{+1.0}_{-0.7}$	4.1 ± 0.2	3.8 ± 0.4	1.01 ± 0.14	683/632
29809–29823	59307	0.94 ± 0.02	2.19 ± 0.04	2.8 ± 0.2	$5.9^{+1.0}_{-0.8}$	3.9 ± 0.3	4.0 ± 0.3	1.08 ± 0.17	708/632
29838–29837	59308	0.75 ± 0.03	2.06 ± 0.04	3.9 ± 0.2	$4.2^{+0.8}_{-0.7}$	4.0 ± 0.3	3.9 ± 0.3	0.98 ± 0.13	710/632
29839–29852	59309	0.73 ± 0.02	1.99 ± 0.04	4.3 ± 0.2	<2.7	3.9 ± 0.3	4.2 ± 0.3	0.91 ± 0.12	699/532
29853–29865	59310	0.74 ± 0.02	1.97 ± 0.04	4.3 ± 0.4	<2.5	3.8 ± 0.4	4.0 ± 0.3	0.91 ± 0.14	717/532

Note. Errors are quoted at 90 per cent confidence (1.6σ).

Table B2. Best-fitting parameters obtained from the spectral fitting of 1 d-averaged data with JETCAF model.

Orbit	MJD	$\dot{m}_d$ ($\dot{m}_{Edd}$)	$\dot{m}_h$ ($\dot{m}_{Edd}$)	X_S (R_g)	R	f_{col}	$\dot{m}_{out}$ ($\dot{m}_{Edd}$)	χ^2/dof
29750–29764	59303	1.87 ± 0.12	0.21 ± 0.05	75.6 ± 6.2	3.50 ± 0.44	0.32 ± 0.05	0.21 ± 0.02	781/625
29765–29778	59304	2.07 ± 0.21	0.24 ± 0.03	57.9 ± 4.6	2.96 ± 0.31	0.31 ± 0.06	0.26 ± 0.06	886/625
29779–29793	59305	1.77 ± 0.15	0.21 ± 0.02	57.3 ± 4.4	3.29 ± 0.21	0.49 ± 0.10	0.33 ± 0.07	899/625
29794–29808	59306	1.77 ± 0.14	0.25 ± 0.06	49.3 ± 5.3	3.66 ± 0.28	0.41 ± 0.09	0.25 ± 0.05	898/625
29809–29823	59307	1.78 ± 0.13	0.25 ± 0.06	49.3 ± 4.9	3.66 ± 0.39	0.39 ± 0.05	0.24 ± 0.02	895/625
29838–29837	59308	1.77 ± 0.08	0.26 ± 0.04	51.6 ± 3.9	3.63 ± 0.32	0.60 ± 0.12	0.37 ± 0.05	897/625
29839–29852	59309	1.91 ± 0.17	0.26 ± 0.06	53.8 ± 5.7	3.30 ± 0.27	0.68 ± 0.15	0.49 ± 0.12	864/625
29853–29865	59310	1.89 ± 0.19	0.26 ± 0.05	52.0 ± 4.5	3.19 ± 0.33	0.73 ± 0.17	0.54 ± 0.13	810/625

Note. Errors are quoted at 90 per cent confidence (1.6σ).

This paper has been typeset from a TEX/LATEX file prepared by the author.